THE JOURNAL OF PHYSICAL CHEMISTRY C
A JOURNAL OF THE AMERICAN CHEMICAL SOCIETY

pubs.acs.org/JPCC

Article

Fragmenting the Kagomé Lattice: Pressure-Tuned Anisotropy of Cu^{2+} Triangles in a Novel Atacamite Relative $CaCu(OH)_3Cl$

Scott D. Ambos, Nicholas S. Manganaro, Matthew DeCapua, Dongzhou Zhang, Phuong Q. H. Nguyen, Jun Yan, and James P. S. Walsh*

Cite This: *J. Phys. Chem. C* 2025, 129, 4226–4232

Read Online

ACCESS | Metrics & More | Article Recommendations | Supporting Information

ABSTRACT: The atacamite family of copper halide minerals contains several prominent quantum spin liquid candidate materials, chiefly herbertsmithite. Unfortunately, an intrinsic chemical disorder in herbertsmithite complicates attempts to perform magneto-structural correlations that deconvolute the fundamental magnetic exchange terms that underpin frustration. We sought to synthesize disorder-free zero-dimensional analogues of the atacamites that retain the basic local geometry required for frustration (i.e., triangular arrangements of spins) while avoiding the extended lattices that are prone to site disorder. We present here the synthesis of a novel trimetallic compound, $CaCu(OH)_3Cl$, that is reminiscent in composition and structure to the known atacamites. $CaCu(OH)_3Cl$ features mildly Jahn–Teller distorted copper triangles that represent zero-dimensional analogues to the triangles that comprise the kagomé layers in herbertsmithite. We present a high-pressure synchrotron single crystal X-ray diffraction study of $CaCu(OH)_3Cl$ up to 10.1(2) GPa and show that pressure counteracts the magnetic Jahn–Teller distortion of the square planar $Cu(OH)_4$ units that comprise the copper triangles, offering a new direction for optimizing magnetic frustration.

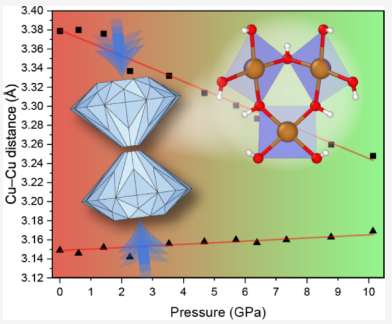

INTRODUCTION

Enormous research effort, both experimental and theoretical, has been directed toward the development and understanding of strongly correlated electronic systems. Of great interest is the long-predicted magnetic phase of matter known as the quantum spin liquid (QSL), which is characterized by strong local electronic interactions and yet resists long-range magnetic order even at 0 K.[1] The QSL phase is underpinned by magnetic frustration (also sometimes referred to as geometric frustration), whereby the local arrangement of magnetic ions on the lattice precludes the system from adopting a single magnetic ground state; even at 0 K, the system fluctuates among a collection of energetically degenerate states. The observation of the QSL phase would represent the second physical realization of a magnetic quantum phenomenon after the fractional quantum Hall effect, and the QSL phase is expected to hold promise in the field of quantum information processing.[2,3] It could also offer new insights related to the mechanisms of unconventional superconductivity.[4,5]

Among the existing QSL candidate materials, the most promising and well-studied to date is the naturally occurring mineral herbertsmithite, $ZnCu_3(OH)_6Cl_2$. Two key attributes of herbertsmithite make it attractive as a QSL host candidate. First, its structure comprises layers of corner-sharing copper triangles arranged in a so-called *kagomé* pattern, which provides the requisite geometry for magnetic frustration.[6] Second, the magnetic ion Cu^{2+} possesses a spin term $S = \frac{1}{2}$, which maximizes quantum interactions. This is in contrast to ions possessing higher total spin quantum number that approach classical behavior.[7−9]

Although herbertsmithite expresses characteristics otherwise ideal for a QSL candidate material, it unfortunately suffers from significant chemical disorder, with ∼10−15% of the interlayer zinc sites being occupied by copper ions.[10] The interlayer coupling introduced by this disorder allows for alternate magnetic exchange pathways that lessen magnetic frustration and effectively poison the QSL phase.[2] While combating this chemical disorder remains a research goal, the intrinsic nature of site defect generation has proven troublesome to counteract, and is exacerbated by the high-temperature synthetic routes for herbertsmithite that engender disorder.[6,10,11]

A metric commonly used to estimate the magnitude of magnetic frustration in materials is the frustration parameter, $f = |\Theta_{CW}|/T_N$, where Θ_{CW} is the Curie–Weiss temperature and T_N is the Néel temperature.[12] The value of f for herbertsmithite is ∼157, which is among the highest measured in any material.[6] Critically, f scales with the strength of the superexchange energy J, which in herbertsmithite is ∼200 K.[13]

Received: November 13, 2024
Revised: November 29, 2024
Accepted: December 2, 2024
Published: December 10, 2024

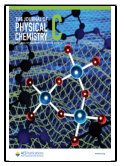

ACS Publications

© 2024 American Chemical Society

Since it has been shown that a high superexchange energy is associated with a high degree of magnetic frustration,[12] the superexchange energy should be maximized in an ideal QSL candidate material.

Previous efforts to improve the fitness of herbertsmithite as a QSL host have focused on cation substitution.[3,14,15] Although this provides rich information on the exchange interaction, one downside is that it renders a discrete (discontinuous) change to the superexchange energy. An alternative approach is the direct modulation of the superexchange interaction through continuous changes to the crystal structure. One method that can achieve this is the application of external pressure, which has the unique capacity to be varied continuously while leaving the composition of the sample unchanged.

We present here a novel copper halide compound, $CaCu(OH)_3Cl$ (**1**), that features a crystal structure composed of isolated Cu^{2+} triangles that are near-perfect structural analogues to those found in the kagomé lattice of herbertsmithite—in essence, zero-dimensional isolated fragments of the herbertsmithite lattice (Figure 1).[6,16] Due to an intrinsic magnetic Jahn−Teller distortion of the square planar $Cu(OH)_4$ constituents of the triangles in Compound **1**, the local arrangement of Cu^{2+} ions deviates from the perfect equilateral triangular structure found in herbertsmithite. We show that under compression up to 10.1(2) GPa, the interatomic Cu−Cu distances and Cu−O−Cu bridging angles follow a trend of convergence, demonstrating that pressure could be used to induce QSL-amenable structure in otherwise distorted materials.

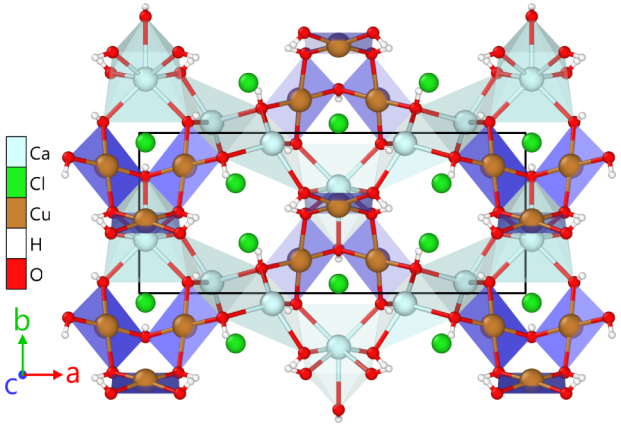

Figure 1. View of the crystal structure of $CaCu(OH)_3Cl$ along the *c*-axis. Colored polyhedra represent local coordination environments.

EXPERIMENTAL SECTION

Synthesis of $CaCu(OH)_3Cl$. Following the methods outlined by Zhu et al. for the synthesis of $SrCu(OH)_3Cl$, $CaCu(OH)_3Cl$ (**1**) was synthesized via an unconventional "solid-state" hydrothermal route.[16] All reagents were purchased from Chem-Impex and used without further purification. In a typical preparation, $CuCl_2$ (1.038 g, 7.721 mmol), $CaCl_2$ (0.415 g, 3.379 mmol), $LiCl{\cdot}H_2O$ (0.415 g, 6.869 mmol), and $LiOH{\cdot}H_2O$ (0.311 g, 7.402 mmol) were added to a 25 mL Teflon liner and agitated by shaking to homogenize the mixture. The Teflon liner was placed in a stainless steel autoclave, which was then sealed and placed in an oven. The vessel was heated from room temperature up to 190 °C at 60 °C/h, held at that temperature for 72 h, and then cooled to 25 °C at 70 °C/h. The product was isolated from the reaction mixture by gravity filtration with sequential washes of deionized water. A typical reaction resulted in single crystals of **1** distributed within a polycrystalline matrix of starting materials and CuO byproducts. Single crystals of **1** appear translucent blue with rectangular prismatic habit, and range in length from 50 to 300 μm, commonly occurring as intergrown clusters. Single crystals of **1** were manually isolated for X-ray diffraction experiments and Raman spectroscopy experiments.

X-ray Diffraction. Single crystal X-ray diffraction was performed on a Rigaku XtaLAB Synergy-S diffractometer equipped with a HyPix-6000HE detector. For low temperature experiments, samples were cooled using an Oxford 800 Series Cryostream Cooler equipped with liquid N_2. Reflections were processed with CrysAlis^{Pro} (Rigaku, ver. 1.171.42.63a), and structural modeling was performed in Olex2 (ver. 1.5) using the SHELXT package.[17,18] Models were refined using the least-squares method of SHELXL.[18]

High-pressure synchrotron single crystal X-ray diffraction was performed at beamline 13-BM-C (GSECARS) at the Advanced Photon Source. For these experiments, three single crystals of **1** were loaded into a symmetric-type diamond anvil cell (DAC) equipped with two diamonds with 300 μm diameter polished culets. The three single crystals were placed in mutually unique orientations to maximize reciprocal space coverage, and two single crystal ruby spheres were added to the sample space as internal pressure calibrants.[19] A stainless steel gasket was indented to ~50 μm and a hole with diameter 210 μm was drilled in the center of the indentation using a Boehler uDriller electrical discharge machining (EDM) tool fitted with a copper wire of appropriate diameter.

During synchrotron diffraction experiments, pressure was increased in the DAC using a gas membrane. For each pressure at which diffraction was to be measured, reflections were measured separately from each of the three single crystals of **1** at a detector angle δ = 0°, and then each experiment was repeated at δ = 25° for a total of six collections per pressure step. Each collection incorporated a ϕ rotation matching the degree measure of the opening aperture—for example, for most collections, the opening aperture was measured to be 66° by observing the maximum angles ϕ at which gasket shadowing was not present. The collection was then set to have a ϕ rotation of 66° with steps of 0.5°/frame and an exposure time of 2 s/frame, for a total of 132 frames over a span of 264 s. Ruby fluorescence was measured before and after each six-experiment sequence, and the average pressure was reported with the standard deviation reported as the error. For all sequences, the difference between the starting and final pressures was between 0.1 and 0.5 GPa. Reflections were collected using a Dectris Pilatus1M area detector. X-rays were tuned to a wavelength of 0.434 Å and the incident X-ray beam focused to an elliptical spot of 12 × 18 μm^2.

Reflections were processed in APEX3 (Bruker, ver. 2022.10-0). Reflections from the three separate crystals were manually sorted into domains and their intensities merged and scaled to produce a final merged reflection file. Structural modeling was performed in Olex2 (ver. 1.5) using the SHELXT package for solution and the least-squares method of SHELXL for refinement.[17,18]

The unit cell parameters, fractional atomic coordinates, and refinement statistics derived from all single crystal diffraction experiments are available in the crystallographic information

https://doi.org/10.1021/acs.jpcc.4c07695
J. Phys. Chem. C 2025, 129, 4226−4232

files deposited with the CCDC under deposition numbers 2379487−2379501 associated with this publication.

Raman Spectroscopy. Raman spectroscopy was performed using a Horiba Jobin Yvon T64000 spectrometer in a single stage configuration (600 lines/mm). The source used was a 3 mW diode-pumped solid-state laser with a wavelength of 532 nm. A single crystal of **1** was manually placed on a glass slide for measurement. Measurements were taken with cross- and cocircular polarization of the laser source.

RESULTS AND DISCUSSION

Crystal Structure. A single crystal X-ray diffraction experiment was performed at ambient temperature and pressure to assign the space group and to solve the structure of **1**. The compound crystallizes in space group $Pmn2_1$ and its structure consists of copper(II) coordination centers in square planar coordination environments with four hydroxyl ligands. For each $Cu(OH)_4$ planar square, two adjacent hydroxyl ligands are bis-coordinated to one neighboring copper(II) center each, forming a triangular arrangement of copper(II) coordination centers with an overall formula of $Cu_3(OH)_9$. This arrangement can be straightforwardly visualized as three squares attached at the corners such that the bounded area is a triangle (Figure 2).

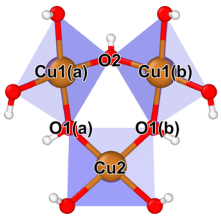

Figure 2. Isolated $Cu_3(OH)_9$ triangle with labeled Cu and O atoms.

Figure 2 illustrates an isolated $Cu_3(OH)_9$ triangular unit. For clarity, only the atoms comprising the core triangle structure are labeled. **Cu1** denotes two copper atoms that are equivalent by symmetry (Wyckoff position *4b*), and **O1** (*4b*) denotes two oxygen atoms that are equivalent by symmetry. The symmetrically unique copper and oxygen atoms are labeled **Cu2** (*2a*) and **O2** (*2a*), respectively.

Each $Cu_3(OH)_9$ triangular unit is coplanar with either the (011) or $(01\bar{1})$ lattice plane, with the orientation of the units switching in ABAB··· fashion along the *a*-axis. Consequently, $Cu_3(OH)_9$ units that are neighbors in the *a*-axis are orthogonal (Figure 1). Each $Cu_3(OH)_9$ unit is linked to its neighbors by a network of calcium(II) coordination centers, and these Ca centers form a repeating chain pattern that is highlighted by the light gray polyhedra in Figure 1. One Ca center occupying Wyckoff position *2a* is heptacoordinated by OH ligands, adopting a distorted tricapped triangular prism geometry with continuous symmetry measure (CSM) = 8.62, indicative of significant distortion from the ideal coordination environment.[20] This calcium center shares two OH ligands with a neighboring tetrahedrally coordinated (CSM = 6.81) Ca center occupying Wyckoff position *4b*, which in turn is connected to an identical and symmetrically equivalent tetrahedral Ca center via two shared OH ligands. The structure is rendered charge-neutral by the presence of chloride anions that occupy the spaces outside of the copper and calcium coordination environments, where they likely stabilize the framework via hydrogen bonding with nearby OH ligands.[16]

1 is isostructural to $SrCu(OH)_3Cl$, a compound first synthesized by Mi et al. in 2014.[16] The title compound and its Sr analogue feature connectivity and composition reminiscent of the atacamite family of minerals, a family well-known to the QSL field for containing herbertsmithite ($ZnCu_3(OH)_6Cl$) among other minerals of interest such as claringbullite ($Cu_4Cl(OH)_7$) and barlowite ($Cu_4BrF(OH)_6$).[21−24] For a comprehensive description of the structure of **1**, we direct the reader to Mi et al.[16] where a detailed discussion of the strontium analogue isostructural to **1** is given.

A motif common to many crystal structures of the atacamite family is a triangle formed by three copper(II) ions linked by hydroxyl groups. In herbertsmithite, these triangles are equilateral (with a Cu−O−Cu angle of 118.87°) and combine through corner-sharing connectivity to form the kagomé layer.[6,25] The strength of the antiferromagnetic superexchange interaction between neighboring hydroxyl-bridged Cu^{2+} ions in herbertsmithite depends primarily on the Cu−O−Cu bridging angle, in accordance with the Goodenough−Kanamori rules.[26,27] The magnitude of magnetic frustration in turn is governed by the strength of this superexchange interaction.[12] Indeed, herbertsmithite has a large frustration parameter $f \approx 157$ compared to Zn-barlowite, for example, which has a Cu−O−Cu bridging angle of ∼117° and $f \approx 25$.[28] It should be noted that the difference in frustration parameter between herbertsmithite and Zn-barlowite is not solely attributable to the Cu−O−Cu bridging angle, but also stems from the combined influence of their differences in structure and composition. While comparisons of the frustration parameter among QSL candidate materials abound, we still lack a clear understanding of the contribution of local distortion to magnetic frustration. To disentangle the effects of distortion, composition, and extended magnetic structure, it is necessary to study the local distortion of a single material with invariant composition and structure.

The crystal structure of **1** features copper-hydroxyl triangles that are very similar to those found in herbertsmithite, but are isosceles rather than equilateral, with a Cu1−O2−Cu1 angle of 107.21(2)° and Cu1−O1−Cu2 angle of 118.63(1)°. The deviation from equilateral geometry is likely the result of a magnetic Jahn−Teller distortion that is not observed in herbertsmithite because of the stabilizing influence of the kagomé layer. Nevertheless, the copper-hydroxyl triangles in **1** represent ideal isolated fragments of the kagomé triangles of herbertsmithite distorted away from ideal geometry, making the system a convenient testbed for studying the relationship between the Cu−O−Cu bridging angle and magnetic frustration.

High-Pressure Synchrotron Single Crystal X-ray Diffraction. In order to examine the structure of **1** under compression, single crystal X-ray diffraction was performed with synchrotron radiation.

The goal of our study—to ascertain bond angles and distances with high precision—necessitated the use of synchrotron radiation for its combination of small spot size, short wavelength, and high photon flux density. Several limitations of high-pressure crystallography—including competing diffraction signal from the gasket material, reflection intensity absorption by the diamond anvils, and poor reciprocal space coverage due to DAC geometry—are mitigated by the aforementioned benefits of the synchrotron source.[29,30]

Single crystals of **1** were studied with X-ray diffraction up to a pressure of 10.1 (2) GPa, with approximately 1 GPa steps in

https://doi.org/10.1021/acs.jpcc.4c07695
J. Phys. Chem. C 2025, 129, 4226−4232

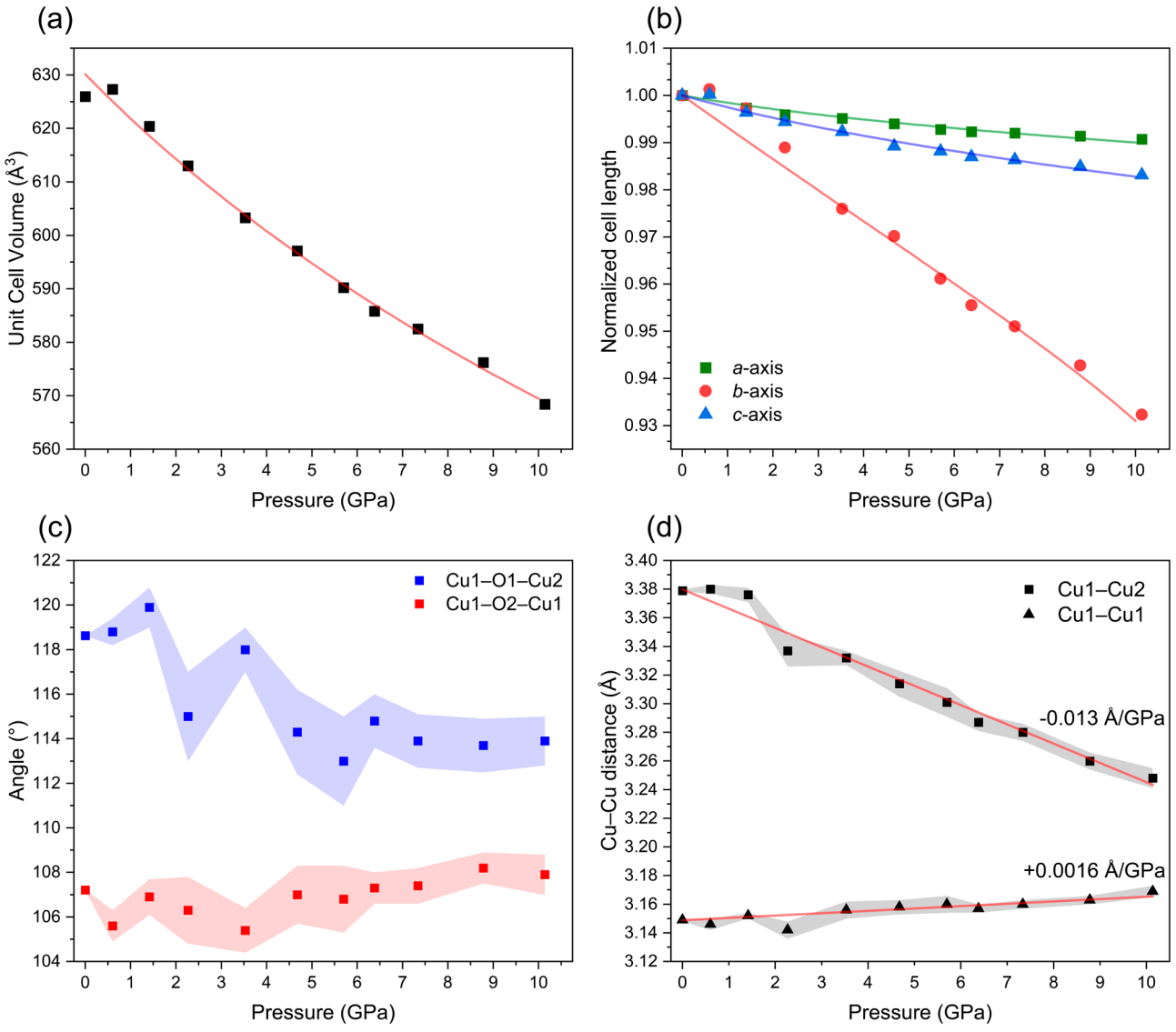

Figure 3. (a) Plot of unit cell volume as a function of pressure. Equation of state fit given in red line. (b) Plot of evolution of lattice parameters as a function of pressure. The cell lengths *a*, *b*, and *c* are normalized to show differences in absolute compressibility. Colored lines show equation of state fits to each axis. In (a) and (b), error bars are smaller than data symbols. (c) Plot of angles Cu1−O1−Cu2 and Cu1−O2−Cu1 as a function of pressure. (d) Plot of Cu1−Cu2 and Cu1−Cu1 distances as a function of pressure. For (c) and (d), the shaded regions represent the estimated standard deviation of each data point.

pressure. Salient parameters extracted from the structural models constructed from each of these diffraction data sets are plotted in Figure 3. Examining the change of the crystallographic axes *a*, *b*, and *c* (Figure 3a), and unit cell volume (Figure 3b) as a function of pressure, a gradual near-linear decrease is observed. Between 0−10.1(2) GPa, the length of the *a*-axis decreases by 0.9%, the *b*-axis by 6.8%, and the *c*-axis by 1.7%. The unit cell volume decreases from a value of 625.97(2) Å^3 at 0 GPa to 568.4(3) Å^3 at 10.1(2) GPa, representing a ∼9.2% decrease. We note that a maximum volume of 627.23(9) Å^3 was observed at 0.6 GPa, which we attribute to differing instrumental parameters between our in-house diffractometer and the synchrotron diffractometer. No discontinuities are observed in any of the unit cell parameters up to the highest pressure studied, and each data set readily indexes to space group $Pmn2_1$, leading us to infer that no phase transition occurred in **1** up to 10.1(2) GPa.

The evolution of the unit cell volume and lattice parameters under compression were fit using third-order Birch−Murnaghan equations of state, yielding a bulk modulus of 72.6 GPa with its first pressure derivative K_p = 6.12.[31] The *a*, *b*, and *c* axes have linear axial moduli of 575.3, 145.4, and 369.1 GPa respectively, reflecting the differences among the three axes in their observed compressibility. The full set of fitted parameters are tabulated in the Supporting Information.

We attempt to rationalize the relatively high compressibility of the *b*-axis by observing the presence of voids in the crystal structure (Figure 1) that are localized in regions not occupied by the copper or calcium coordination centers, and are of maximum dimension along the *b*-axis. These voids represent areas where we would expect to observe the greatest contraction under compression, and it follows that the *b* axis is less rigid than the *a* and *c*-axes.

Figure 3c plots the change in the Cu1−O1−Cu2 and Cu1−O2−Cu1 bridging angles (see Figure 2) under compression.

https://doi.org/10.1021/acs.jpcc.4c07695
J. Phys. Chem. C 2025, 129, 4226−4232

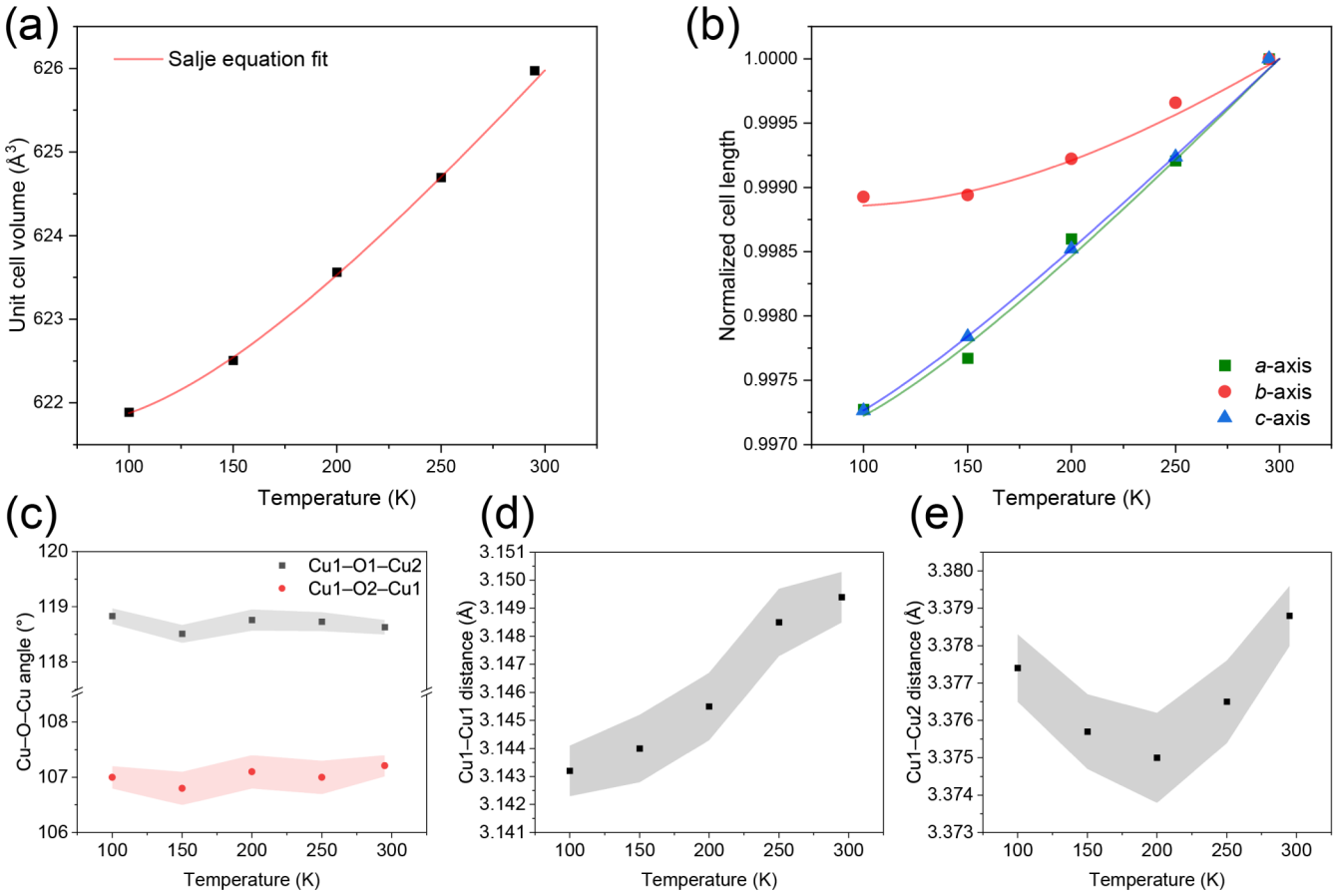

Figure 4. (a) Unit cell volume as a function of temperature down to 100 K. The red line represents the fit to the data given by the Salje equation of saturation of thermal expansion. (b) Normalized unit cell parameters as a function of temperature down to 100 K. Error bars are smaller than data symbols. Lines represent the fits of the Salje equation of saturation of thermal expansion. (c) Angles Cu1−O2−Cu1 and Cu1−O1−Cu2 as a function of temperature. (d) Cu1−Cu1 distance as a function of temperature. (e) Cu1−Cu2 distance as a function of temperature. For (c), (d), and (e), the shaded areas represent the estimated standard deviation of each data point.

The angle Cu1−O1−Cu2 has a value of 118.63(1)° at 0 GPa and decreases gradually to a value of 114(1)° at 10.1(2) GPa. Conversely, angle Cu1−O2−Cu1 is seen to gradually increase over the pressure range, from 107.21(2)° at 0 GPa to 107.9(9)° at 10.1(2) GPa. It should be noted that the Cu1−O1−Cu2 bridging angle responds quite drastically to compression compared to the Cu1−O2−Cu1 bridging angle, experiencing a decrease of 4.7° compared to a 0.7° increase in the Cu1−O2−Cu1 bridging angle.

A similar trend is apparent in Figure 3d, which plots the change of the two initially inequivalent Cu−Cu distances under compression. The Cu−Cu distance is inextricably linked to the Cu−O−Cu bridging angle, so their mirrored behavior under compression is expected. The Cu1−Cu2 distance at 0 GPa is 3.3790(8) Å, decreasing under compression to 3.248(7) Å at 10.1(2) GPa. The opposite behavior is observed for the Cu1−Cu1 distance, which at 0 GPa is 3.1490(9) Å, increasing to 3.169(4) Å at 10.1(2) GPa.

A separate set of single crystal diffraction experiments were performed at ambient pressure and at 300, 250, 200, 150, and 100 K to assess the thermal expansion properties of **1** (See Figure 4). The unit cell volumes obtained from these experiments were fit using the Salje equation for the saturation of thermal expansion at low temperature and yielded a volumetric thermal expansion coefficient $\alpha_V = 4.6 \times 10^{-5}$ K^{-1} and a saturation temperature $\Theta_{sat} = 203.06$ K.[31−33] This value of α_V fits in the expected range of values typically observed for crystalline solids.[34,35] We note that low temperature has a comparatively minuscule effect on the unit cell volume, lattice parameters, and salient bond distances and angles in **1**. Down to 100 K, the unit cell volume contracts by only ∼0.65%, while the *a*-, *b*-, and *c*-axes contract by ∼0.27%, ∼0.11%, and ∼0.27% respectively (Figure 4a,b). Similarly, we find the Cu1−O2−Cu1 and Cu1−O1−Cu2 bridging angles to be virtually invariant across the temperature range studied (Figure 4c). The Cu1−Cu1 distance is observed to decrease by 0.0062 Å (0.2%) and the Cu1−Cu2 distance by 0.0014 Å (0.04%) (Figure 4d,e). Despite the overall decrease in the Cu1−Cu2 distance down to 100 K, a pronounced saddle shape is observed, showing a minimum Cu1−Cu2 distance around 200 K. We note a concomitant leveling-off of the *b*-axis length around 200 K, suggesting that these structural responses to cooling may be related. For all of the structural properties of interest, we show that pressure has a far greater effect than temperature—it is a favorable property of any QSL candidate material to be structurally robust to low temperature, as magnetic measurements are routinely performed in the low temperature regime where paramagnetism is suppressed.

The conclusion that can be drawn from these data is that pressure acts counter to the magnetic Jahn−Teller effect that causes the distortion of the $Cu_3(OH)_9$ triangle. This result is in good agreement with measurements of the high-pressure

https://doi.org/10.1021/acs.jpcc.4c07695
J. Phys. Chem. C 2025, 129, 4226−4232

structural behavior of clinoatacamite, where pressure has been found to act against the intrinsic Jahn−Teller distortion of the $Cu(OH)_6$ octahedra.[36] The apparent convergence of parameters suggests that at some higher pressure they may be rendered equal, although the possibility of a phase transition before such a convergence remains. Based on linear fits of the Cu1−Cu1 and Cu1−Cu2 distances under compression (Figure 3c), we would expect these distances to converge at a pressure of ∼15.6 GPa. Linear fits of the Cu1−O1−Cu2 and Cu1−O2−Cu1 angles under compression, while less reliable due to the nonlinearity and variance of the data, yield a convergence pressure of ∼20 GPa, which is in reasonable agreement with the estimate based on distances. The linear fits of the Cu−O−Cu angles indicate that the angles Cu1−O2−Cu1 and Cu1−O1−Cu2 are converging to a value of 107.2°. At this convergence angle, we would expect the $Cu_3(OH)_9$ cyclic trimers to exhibit relatively strong spin frustration. Seeking a comparison with materials already reported in the literature, we highlight $CdCu_3(OH)_6(NO_3)_2$, a kagomé antiferromagnet based on corner-sharing $Cu_3(OH)_9$ triangles, where the bridging angle of Cu−O−Cu cyclic trimers is 106.4°, a value close to the convergence angle we predict in $CaCu(OH)_3Cl$ under pressure. In $CdCu_3(OH)_6(NO_3)_2$ the Curie−Weiss temperature was found to be $\Theta_{CW} = -114 \pm 27$ K , indicative of strong antiferromagnetic exchange.[37]

CONCLUSIONS

In summary, we have presented the synthesis of $CaCu(OH)_3Cl$, a novel copper halide featuring composition and structure similar to compounds in the atacamite family of minerals. The isolated $Cu_3(OH)_9$ triangles found in $CaCu(OH)_3Cl$ are close structural analogues of the triangles that comprise the kagomé layer in herbertsmithite, differentiated only by an intrinsic Jahn−Teller distortion in the case of $CaCu(OH)_3Cl$. We have leveraged synchrotron single crystal X-ray diffraction to show how pressure counteracts the Jahn−Teller distortion, with both the Cu−O−Cu bridging angle and Cu−Cu distance following a trend of convergence.

These results highlight an unexplored path toward the enhancement of QSL candidates, showing how phases that are disqualified from consideration due to significant distortions away from ideal lattices could be brought "into compliance" through the application of extreme pressure. This could open up a new avenue of exploration targeting otherwise promising phases and using extreme pressure to engender magnetic frustration, for example in other spin liquid candidates that exhibit structural distortions, such as $Ba_3CuSb_2O_9$[38] and $Ca_{10}Cr_7O_{28}$.[39]

ASSOCIATED CONTENT

Supporting Information

The Supporting Information is available free of charge at https://pubs.acs.org/doi/10.1021/acs.jpcc.4c07695.

Optical microscope image of single crystal of **1**; cross- and cocircularly polarized Raman spectra of **1**; parameters of equation of state fits to pressure data; tabulated experimental pressures, unit cell volumes, and lattice parameters (PDF)

AUTHOR INFORMATION

Corresponding Author

James P. S. Walsh − *Department of Chemistry, University of Massachusetts Amherst, Amherst, Massachusetts 01003, United States;* orcid.org/0000-0003-3454-3428; Email: jpswalsh@umass.edu

Authors

Scott D. Ambos − *Department of Chemistry, University of Massachusetts Amherst, Amherst, Massachusetts 01003, United States;* orcid.org/0000-0001-9898-5626

Nicholas S. Manganaro − *Department of Chemistry, University of Massachusetts Amherst, Amherst, Massachusetts 01003, United States;* orcid.org/0000-0002-2772-8769

Matthew DeCapua − *Department of Physics, University of Massachusetts Amherst, Amherst, Massachusetts 01003, United States*

Dongzhou Zhang − *GSECARS, University of Chicago, Chicago, Illinois 60439, United States;* orcid.org/0000-0002-6679-892X

Phuong Q. H. Nguyen − *GSECARS, University of Chicago, Chicago, Illinois 60439, United States*

Jun Yan − *Department of Physics, University of Massachusetts Amherst, Amherst, Massachusetts 01003, United States;* orcid.org/0000-0003-3861-4633

Complete contact information is available at: https://pubs.acs.org/10.1021/acs.jpcc.4c07695

Notes

The authors declare no competing financial interest.

ACKNOWLEDGMENTS

We gratefully acknowledge the University of Massachusetts Amherst for startup funding. Portions of this work were performed at GeoSoilEnviroCARS (The University of Chicago, Sector 13), Advanced Photon Source (APS), Argonne National Laboratory. GeoSoilEnviroCARS was supported by the National Science Foundation − Earth Sciences (EAR − 1634415). This research used resources of the Advanced Photon Source, a U.S. Department of Energy (DOE) Office of Science User Facility operated for the DOE Office of Science by Argonne National Laboratory under Contract No. DE-AC02-06CH11357. Raman spectroscopy was supported by the National Science Foundation (DMR-2004474).

REFERENCES

(1) Anderson, P. W. Resonating valence bonds: A new kind of insulator? *Mater. Res. Bull.* **1973**, *8*, 153−160.

(2) Broholm, C.; Cava, R. J.; Kivelson, S. A.; Nocera, D. G.; Norman, M. R.; Senthil, T. Quantum Spin Liquids. *Science* **2020**, *367*, No. eaay0668.

(3) Chamorro, J. R.; McQueen, T. M.; Tran, T. T. Chemistry of quantum spin liquids. *Chem. Rev.* **2021**, *121*, 2898−2934.

(4) Quintanilla, J.; Hooley, C. The strong-correlations puzzle. *Phys. World* **2009**, *22*, 32.

(5) Keimer, B.; Moore, J. The physics of quantum materials. *Nat. Phys.* **2017**, *13*, 1045−1055.

(6) Shores, M. P.; Nytko, E. A.; Bartlett, B. M.; Nocera, D. G. A structurally perfect S= 1/2 kagome antiferromagnet. *J. Am. Chem. Soc.* **2005**, *127*, 13462−13463.

(7) Waldtmann, C.; Everts, H.-U.; Bernu, B.; Lhuillier, C.; Sindzingre, P.; Lecheminant, P.; Pierre, L. First excitations of the

spin 1/2 Heisenberg antiferromagnet on the kagomé lattice. *Eur. Phys. J. B* **1998**, *2*, 501−507.
(8) Mambrini, M.; Mila, F. RVB description of the low-energy singlets of the spin 1/2 kagomé antiferromagnet. *Eur. Phys. J. B* **2000**, *17*, 651−659.
(9) Hastings, M. Dirac structure, RVB, and Goldstone modes in the kagomé antiferromagnet. *Phys. Rev. B* **2000**, *63*, 014413.
(10) Freedman, D. E.; Han, T. H.; Prodi, A.; Muller, P.; Huang, Q.-Z.; Chen, Y.-S.; Webb, S. M.; Lee, Y. S.; McQueen, T. M.; Nocera, D. G. Site specific X-ray anomalous dispersion of the geometrically frustrated kagomé magnet, herbertsmithite, $ZnCu_3(OH)_6Cl_2$. *J. Am. Chem. Soc.* **2010**, *132*, 16185−16190.
(11) Chu, S.; Müller, P.; Nocera, D. G.; Lee, Y. S. Hydrothermal growth of single crystals of the quantum magnets: Clinoatacamite, paratacamite, and herbertsmithite. *Appl. Phys. Lett.* **2011**, *98*, 092508.
(12) Ramirez, A. Strongly geometrically frustrated magnets. *Annu. Rev. Mater. Sci.* **1994**, *24*, 453−480.
(13) Fu, M.; Imai, T.; Han, T.-H.; Lee, Y. S. Evidence for a gapped spin-liquid ground state in a kagome Heisenberg antiferromagnet. *Science* **2015**, *350*, 655−658.
(14) Norman, M. Colloquium: Herbertsmithite and the search for the quantum spin liquid. *Rev. Mod. Phys.* **2016**, *88*, 041002.
(15) Nytko, E. A. *Synthesis, structure, and magnetic properties of spin-1/2 kagomé antiferromagnets*, PhD. Thesis, MIT Libraries, 2008.
(16) Zhu, T.-T.; Sun, W.; Huang, Y.-X.; Sun, Z.-M.; Pan, Y.; Balents, L.; Mi, J.-X. Strong spin frustration from isolated triangular Cu (II) trimers in $SrCu(OH)_3Cl$ with a novel cuprate layer. *J. Mater. Chem. C* **2014**, *2*, 8170−8178.
(17) Dolomanov, O. V.; Bourhis, L. J.; Gildea, R. J.; Howard, J. A.; Puschmann, H. OLEX2: A complete structure solution, refinement and analysis program. *J. Appl. Crystallogr.* **2009**, *42*, 339−341.
(18) Sheldrick, G. M. SHELXT−Integrated space-group and crystal-structure determination. *Acta Crystallogr., Sect. A: Found. Adv.* **2015**, *71*, 3−8.
(19) Tchoń, D.; Makal, A. Maximizing completeness in single-crystal high-pressure diffraction experiments: Phase transitions in 2° AP. *IUCr J.* **2021**, *8*, 1006−1017.
(20) Zabrodsky, H.; Peleg, S.; Avnir, D. Continuous symmetry measures. *J. Am. Chem. Soc.* **1992**, *114*, 7843−7851.
(21) Henderson, A.; Dong, L.; Biswas, S.; Revell, H. I.; Xin, Y.; Valenti, R.; Schlueter, J. A.; Siegrist, T. Order−disorder transition in the S= kagome antiferromagnets claringbullite and barlowite. *Chem. Commun.* **2019**, *55*, 11587−11590.
(22) Tustain, K.; Ward-O'Brien, B.; Bert, F.; Han, T.; Luetkens, H.; Lancaster, T.; Huddart, B. M.; Baker, P. J.; Clark, L. From magnetic order to quantum disorder in the Zn-barlowite series of S= 1/2 kagomé antiferromagnets. *npj Quantum Mater.* **2020**, *5*, 74.
(23) Georgopoulou, M.; Fåk, B.; Boldrin, D.; Stewart, J. R.; Ritter, C.; Suard, E.; Ollivier, J.; Wills, A. Magnetically ordered and kagome quantum spin liquid states in the Zn-doped claringbullite series. *Phys. Rev. B* **2023**, *107*, 024416.
(24) Feng, Z.; Yi, W.; Zhu, K.; Wei, Y.; Miao, S.; Ma, J.; Luo, J.; Li, S.; Meng, Z. Y.; Shi, Y. From claringbullite to a new spin liquid candidate $Cu_3Zn(OH)_6FCl$. *Chin. Phys. Lett.* **2018**, *36*, 017502.
(25) Kozlenko, D.; Kusmartseva, A. F.; Lukin, E.; Keen, D.; Marshall, W.; De Vries, M.; Kamenev, K. V. From quantum disorder to magnetic order in an S= 1/2 kagome lattice: A structural and magnetic study of herbertsmithite at high pressure. *Phys. Rev. Lett.* **2012**, *108*, 187207.
(26) Goodenough, J. B. Theory of the role of covalence in the perovskite-type manganites [La,*M*(II)]MnO_3. *Phys. Rev.* **1955**, *100*, 564.
(27) Kanamori, J. Theory of the magnetic properties of ferrous and cobaltous oxides, I. *Prog. Theor. Phys.* **1957**, *17*, 177−196.
(28) Smaha, R. W.; He, W.; Jiang, J. M.; Wen, J.; Jiang, Y.-F.; Sheckelton, J. P.; Titus, C. J.; Wang, S. G.; Chen, Y.-S.; Teat, S. J.; et al. Materializing rival ground states in the barlowite family of kagome magnets: Quantum spin liquid, spin ordered, and valence bond crystal states. *npj Quantum Mater.* **2020**, *5*, 23.
(29) Angel, R. J.; Milani, S.; Alvaro, M.; Nestola, F. High-quality structures at high pressure? Insights from inclusions in diamonds. *Z. Fur Krist. -Cryst. Mater.* **2016**, *231*, 467−473.
(30) Angel, R. J.; Downs, R. T.; Finger, L. W. High-temperature−high-pressure diffractometry. *Rev. Mineral. Geochem.* **2000**, *41*, 559−597.
(31) Angel, R. J.; Alvaro, M.; Gonzalez-Platas, J. EosFit7c and a Fortran module (library) for equation of state calculations. *Z. Fur Krist. -Cryst. Mater.* **2014**, *229*, 405−419.
(32) Salje, E. K. H. Crystallography and structural phase transitions, an introduction. *Acta Crystallogr., Sect. A: Found. Crystallogr.* **1991**, *47*, 453−469.
(33) Salje, E. K. H.; Wruck, B.; Thomas, H. Order-parameter saturation and low-temperature extension of Landau theory. *Z. Phys. B: Condens. Matter* **1991**, *82*, 399−404.
(34) Neumann, H. Trends in the thermal expansion coefficients of the $A^IB^{III}C_2^{VI}$ and $A^{II}B^{IV}C_2^{V}$ chalcopyrite compounds. *Krist. Tech.* **1980**, *15*, 849−857.
(35) Zhao, Y.; Weidner, D. J. Thermal expansion of $SrZrO_3$ and $BaZrO_3$ perovskites. *Phys. Chem. Miner.* **1991**, *18*, 294−301.
(36) Luo, Y.; Zhang, J.; Tian, H.; Wang, Y.; Cui, H.; Ma, Y.; Cui, Q. Interplay between external high pressure and intrinsic Jahn−Teller effect in the compression behavior of clinoatacamite. *Inorg. Chem.* **2022**, *61*, 6869−6880.
(37) Nytko, E. A.; Shores, M. P.; Helton, J. S.; Nocera, D. G. $CdCu_3(OH)_6(NO_3)_2$: An S= 1/2 Kagomé Antiferromagnet. *Inorg. Chem.* **2009**, *48*, 7782−7786.
(38) Drichko, N.; Broholm, C.; Kimura, K.; Ishii, R.; Nakasutji, S. Collective versus local Jahn-Teller distortion in $Ba_3CuSb_2O_9$: Raman scattering study. *Phys. Rev. B* **2016**, *93*, 184425.
(39) Balz, C.; Lake, B.; Reuther, J.; Luetkens, H.; Schönemann, R.; Herrmannsdörfer, T.; Singh, Y.; Nazmul Islam, A. T. M.; Wheeler, E. M.; Rodriguez-Rivera, J. A.; et al. Physical realization of a quantum spin liquid based on a complex frustration mechanism. *Nat. Phys.* **2016**, *12*, 942−949.

https://doi.org/10.1021/acs.jpcc.4c07695
J. Phys. Chem. C 2025, 129, 4226−4232